energies

MDPI

Article

Quantitative Prediction of Rock Pore-Throat Radius Based on Deep Neural Network

Yao Hong [1], Shunming Li [2], Hongliang Wang [1,*], Pengcheng Liu [1] and Yuan Cao [3]

[1] School of Energy Resources, China University of Geosciences, Beijing 100083, China; arthuricier@outlook.com (Y.H.); lpc@cugb.edu.cn (P.L.)
[2] Research Institute of Petroleum Exploration and Development, PetroChina, Beijing 100083, China; leesm@petrochina.com.cn
[3] Shanxi Coalbed Methane Branch of Huabei Oilfield Company, PetroChina, Jincheng 048000, China; mcq_caoyuan@petrochina.com.cn
* Correspondence: whliang@cugb.edu.cn; Tel.: +86-010-82321865

Abstract: Pore-throat radius is one of the key parameters that characterizes the microscopic pore structure of rock, which has an important impact on oil-gas seepage and the prediction of remaining oil's microscopic distribution. Currently, the quantitative characterization of a pore-throat radius mainly relies on rock-core experiments, then uses capillary pressure functions, e.g., the J-function, to predict the pore-throat radius of rocks which have not undergone core experiments. However, the prediction accuracy of the J-function struggles to meet the requirements of oil field development during a high water-cut stage. To solve this issue, in this study, based on core experimental data, we established a deep neural network (DNN) model to predict the maximum pore-throat radius R_{max}, median pore-throat radius R_{50}, and minimum flow pore-throat radius R_{min} of rocks for the first time. To improve the prediction accuracy of the pore-throat radius, the key components of the DNN are preferably selected and the hyperparameters are adjusted, respectively. To illustrate the effectiveness of the DNN model, core samples from Q Oilfield were selected as the case study. The results show that the evaluation metrics of the DNN notably outperform when compared to other mature machine learning methods and conventional J-function method; the root-mean-square error (RMSE), mean absolute error (MAE), and mean absolute percentage error (MAPE) are decreased by 14–57.8%, 32.4–64.3% and 13.5–48.9%, respectively, and the predicted values are closer to the true values of the pore-throat radius. This method provides a new perspective on predicting the pore-throat radius of rocks, and it is of great significance for predicting the dominant waterflow pathway and in-depth profile control optimization.

Keywords: pore-throat radius; deep neural network; hyperparameter optimization; J-function; quantitative characterization

check for updates

Citation: Hong, Y.; Li, S.; Wang, H.; Liu, P.; Cao, Y. Quantitative Prediction of Rock Pore-Throat Radius Based on Deep Neural Network. *Energies* **2023**, *16*, 7277. https://doi.org/10.3390/en16217277

Academic Editors: Hossein Hamidi, Krzysztof Skrzypkowski and Chun Zhu

Received: 19 September 2023
Revised: 9 October 2023
Accepted: 24 October 2023
Published: 26 October 2023

Copyright: © 2023 by the authors. Licensee MDPI, Basel, Switzerland. This article is an open access article distributed under the terms and conditions of the Creative Commons Attribution (CC BY) license (https://creativecommons.org/licenses/by/4.0/).

1. Introduction

Since the 1970s, the quantitative characterization of reservoir heterogeneity has been widely focused on by geologists and reservoir engineers [1–3]. The microscopic heterogeneity of a reservoir includes pore-throat type, size, interconnectivity, and uniformity [4]. The pore-throat radius, as one of the key parameters for characterizing microscopic heterogeneity, directly affects the storage and seepage of oil-gas, the remaining oil distribution, and the optimization of in-depth profile control [5]. The maximum pore-throat radius R_{max}, the median pore-throat radius R_{50}, and the minimum flow pore-throat radius R_{min} are three important evaluation parameters for characterizing the pore-throat radius of rocks. The maximum pore-throat radius can assist in reservoir evaluation and selecting plugging agents in the oil-production stage [6]; the median pore-throat radius approximately represents the average pore-throat space size of the rock and can be used for reservoir permeability prediction [7,8]; the minimum flow pore-throat radius reflects the difficulty of

oil and gas filling [9] and the lower limit of petrophysical properties [10]. The three radii comprehensively characterize the reservoir's storage and seepage capacity.

Currently, there are two types of characterization methods for the pore-throat radius, i.e., core-based characterization and petrophysics-based characterization. Core-based characterization relies on experimental and imaging analyses directly on core samples, such as the mercury-injection–capillary-pressure (MICP) test and thin sections revealing the size and distribution of key parameters. Petrophysics-based characterization is used to predict the size of the pore-throat radius by establishing the petrophysical parameter model.

Core-based characterization can be divided into three categories: two-dimensional image observation, quantitative experimental characterization, and three-dimensional digital core analysis. The two-dimensional image observation method uses optical microscopy, scanning electron microscopy, field-emission scanning electron microscopy, atomic force microscopy, et cetera, to identify the characteristics of pore structures [11–15]. However, it is inefficient and relies on the professional ability and subjective understanding of researchers. Quantitative experimental characterization methods include the mercury-injection–capillary-pressure test, nitrogen adsorption, and nuclear magnetic resonance, which can accurately identify the micro-mesoscopic pore-throat features of reservoir rocks [16,17], the distribution characteristics of reservoir fluids [18], and fracture strike [19]. These methods are relatively mature, but there are still shortcomings such as small measuring range, sample damage, and environmentally unfriendly impacts. Digital core is a three-dimensional digital model based on real core samples [20,21], which is a repeatable, efficient, and non-destructive way to characterize the microscopic pore-throat distribution. High accuracy is achieved by physical experimental methods such as focused ion microscopy and micro/nano CT scanning to obtain digital cores [22–24], but it is costly and time-consuming. Digital cores built by geostatistical methods [25] mainly match the statistical characteristics of microscopic pores in real cores, but are isotropic. Based on the digital core model, many scholars have been working on new theoretical methods including the maximal ball method [26,27], percolation theory [28], pathfinding approach [29], medial axis extraction algorithm [30] and watershed segmentation algorithm [31], to build a pore network model that reflects the topology of real pore space. All the methods mentioned above have their own specific characterization ranges and scales; in order to obtain a more realistic and overall pore-throat distribution, comprehensive experimental methods for characterizing the full pore-size distribution have become the mainstream in recent years [32–34]. As we can see, the core-based characterization methods are based on actual core samples, and the results obtained are only for those samples. It is not possible to predict the pore-throat radius of rocks that have not been sampled or scanned.

Petrophysics-based characterization methods can predict the pore-throat radius. Some scholars have provided a classical capillary pressure curve fitting method [35,36]. Several scholars have established empirical fitting formulae for the pore-throat radius R_{35} using petrophysical parameters such as porosity and permeability [37–39]. Xiao et al., proposed a synthetic approach for calculating the bound water film thickness of pore structures; then, the pore-throat radius is predicted indirectly [10]. Although these characterization methods can predict the pore-throat radius, there is still room for improvement in prediction accuracy.

In recent years, machine learning and deep learning applications are increasing by leaps and bounds in the field of engineering disciplines. Deep learning is more structurally complex and establishes more realistic mapping relationships. It has been widely used in petroleum exploration and development fields such as geophysics [40], reservoir characterization [41], and oil-gas field development [42]. The No Free Lunch Theorem (NFLT) [43] for machine learning shows that no machine learning algorithm can significantly outperform other algorithms on all issues, that is, different algorithms have a certain range of applicability. For instance, a deep neural network (DNN), which is adept in processing data, is used to predict geomechanical parameters [44]. A convolutional neural network (CNN), which is good at extracting high-dimensional image features, is used to predict lithofacies and pore

types [45,46]. A long short-term memory (LSTM) network, which can deal with temporal relationships, is proposed for well log generation [47,48]. A generative adversarial network (GAN), which is good at extracting image patterns, is introduced in modeling reservoir sedimentary facies [49,50]. Currently, in regard to petrophysical characterization and microscopic heterogeneity, many machine learning methods have been devoted to generating more accurate predictions. Lu et al. [51] predicted the pore structure type of the carbonate reservoirs in the Iraq H oilfield by using Gradient Boost Decision Trees and Support Vector Regression. In the procedure of analyzing the permeability contribution of multiscale pore structure, Wang and Sun [52] classified a multiscale pore structure into different rock types using the Random Forest algorithm. Pan et al. [53] proposed an optimized XGBoost method for predicting reservoir porosity. As for deep learning, convolutional neural networks are widely used based on two-dimensional CT core images; Alqahtani et al. [54,55] predicted the porosity, specific surface area, coordination number and average pore size of sandstone by employing the CNN method. Misbahuddin [56] predicted the porosity and average pore size of Marcellus shale with the CNN method, accelerated the process of SEM-image analysis, and reduced the computational cost. Iraji et al. [57] characterized reservoir rock types of carbonate reservoirs in the Santos Basin by the unsupervised learning method, and predicted porosity and permeability by implementing the ResNet model and 1D CNN. As can be seen, most of the studies focus on the classification of discrete variables such as pore-structure types and the prediction of continuous variables such as petrophysical properties. There are few studies of the deep learning domain on predicting rock pore-throat radius. For clarity, we summarize the relevant methods for predicting pore-throat radius in Table 1.

Table 1. The relevant methods for predicting pore-throat radius.

	Method	Input Variable	Prediction	Source
Petrophysics-based Methods	empirical fitting formulae	porosity, permeability	R_{35}	[37–39]
	Indirect prediction by bound water film thickness	bound water volume, inner surface area	lower limits of pore-throat radius	[10]
Machine learning Methods	5 layers CNN	micro-CT images	average pore size	[54,55]
	4 layers CNN	grayscale SEM images	average pore size	[56]
	componential optimized deep neural network	lithology, porosity, permeability, and shale volume	R_{max}, R_{50} and R_{min}	This paper

Under the long-term impact of geological processes, including sedimentation, diagenesis, and tectonic activity, there is a complex nonlinear correlation between the pore-throat radius and other geological parameters. Relying on a simple regression fitting formula, the accuracy of predicting the pore-throat radius is relatively low. In this study, we develop a deep neural network combining petrophysical analysis to address the above shortcomings. To the best of the authors' knowledge, the quantitative prediction of the maximum pore-throat radius, median pore-throat radius, and minimum flow pore-throat radius is achieved for the first time by a componential optimized deep neural network. We have adopted a mass of rock-core experimental data to evaluate the method. The evaluation metrics. including mean absolute error (MAE), root-mean-square error (RMSE), and mean absolute percentage error (MAPE), together with actual prediction results, show that the DNN outperforms conventional machine learning methods and the J-function method by a wide margin, indicating that DNN prediction is significantly more accurate and is less time-consuming. This paper is organized as follows. We briefly introduce the data sources and platform support in Section 2. Then, we detail the process of predicting the pore-throat radius using the DNN in Section 3. Finally, we evaluate the methods and discuss the corresponding results in Section 4. In Section 5, we summarize the conclusions of the study.

2. Materials

The core experimental data utilized are from Q Oilfield, a mainly continental sandstone reservoir which is located in Songliao basin, northeastern China. The oil-rich cretaceous Qingshankou Formation, Yaojia Formation, and Nenjiang Formation are the main producing reservoirs, and they are also the sources of our core samples. After long-term development, a large amount of core experimental analysis data has been accumulated. We established a reservoir parameter database containing over 88,000 core samples by analyzing rock grain-size data, conventional petrophysical data, and high-pressure MICP data from 163 coring wells, among which, 20.1%, 75% and 4.9% of the core samples are located in the Qingshankou Formation, Yaojia Formation, and Nenjiang Formation, respectively. Based on data quality-control and petrophysical analysis, the dataset for the pore-throat radius prediction was further selected.

According to the type and amount of core data available for this research, together with the aforementioned No Free Lunch Theorem, the Deep Neural Network was selected. The experimental platform adopted here is the mainstream deep learning framework TensorFlow 2.10.0, and the programming language is Python 3.9.

3. Method

The procedure of predicting the pore-throat radius by deep neural networks (Figure 1) includes data analysis and preprocessing; building, adjustment and optimizing of deep neural network; prediction results evaluation.

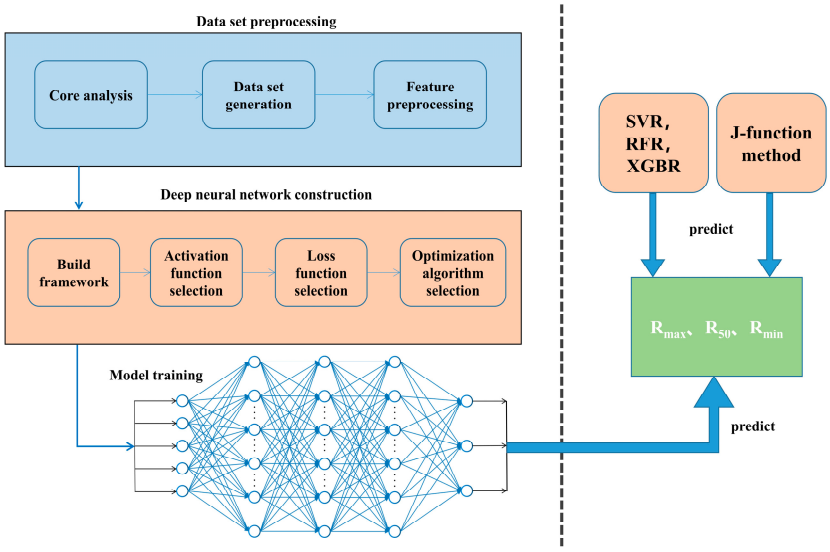


Figure 1. The workflow of pore-throat radius prediction in this study.

3.1. Data Analysis and Preprocessing

The pore-throat radius and other geological parameters have a complex high-dimensional nonlinear mapping relationship. According to the established database of the study area and the previous studies of predecessors [36,38,45], four types of parameters, including lithology, porosity, permeability, and shale volume, were selected as input features of the DNN model.

Generally, the coarser the grain size of sandstone is, the larger the pore-throat radii are. According to the grain-size data which achieved via sieve analysis and the thin-section analysis method, the sandstone in the study area can be subdivided into five types: medium sandstone, fine sandstone, siltstone, unequal-grained sandstone, and diamictite. The range of median grain size of each lithology is shown in Table 2. The lithology of the study area is mainly composed of fine sandstone and siltstone, accounting for 70% in total (Figure 2).

Table 2. Median grain size of each lithology.

Lithology	Medium Sandstone	Fine Sandstone	Siltstone	Unequal-Grained Sandstone	Diamictite
Median grain size (μm)	235–344	86–245	11–98	101–261	29–162

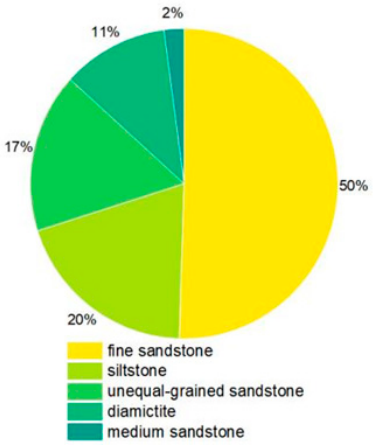


Figure 2. Lithology statistics of the study area.

Porosity, permeability, and shale volume are indirectly connected to the size of the pore-throat radius. After sorting out, there were over 88,000 groups of petrophysical property data in the study area. Combined with previous research [58], we filtered porosity, permeability, and shale volume data, and outliers were deleted. The box plots (Figure 3) shows that porosity, permeability, and shale volume have an obvious matching relationship with lithology. As the rock grain-size becomes thicker, the main distribution range of porosity and permeability gradually rises. There is a certain correlation between porosity and permeability of the same lithology, indicating the impact of complex pore-throat radius distribution.

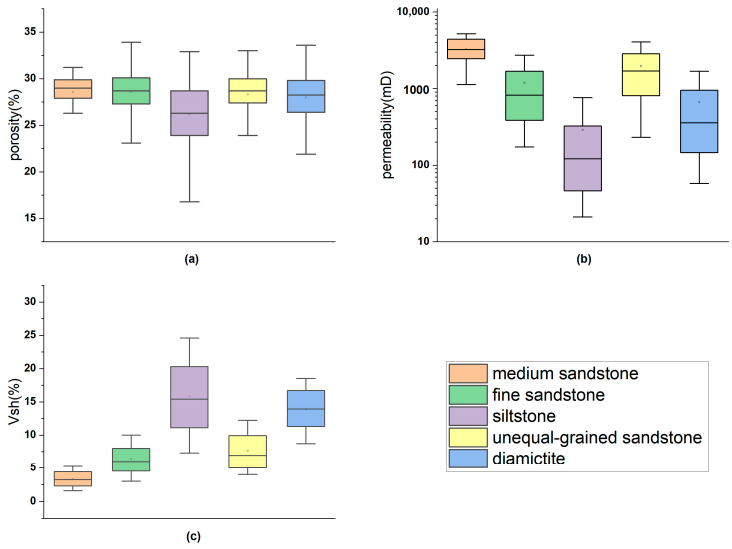


Figure 3. The box plots of geological parameters in the study sorted by lithology. (**a**) Porosity, (**b**) permeability, (**c**) shale volume.

The prerequisite for effective prediction of the pore-throat radius is to obtain sufficient pore-throat radius samples to train, validate, and test the deep neural network. The maximum pore-throat radius R_{max} and the median pore-throat radius R_{50} are, respectively, corresponding to the threshold pressure P_T at which non-wetting phase fluids begin to

enter the core in MICP experiments, and the median pressure P_{c50} when non-wetting phase fluid saturation reaches 50%. The relationship between pore-throat radius and capillary pressure can be calculated by Washburn's equation [59] (Equation (1)).

$$r = \frac{2\gamma \cos\theta}{P_c} \tag{1}$$

where r is pore-throat radius, γ is surface tension, θ is contact angle, and P_c is capillary pressure.

Based on 5722 groups of MICP data obtained from core samples in the study area, the corresponding R_{max} and R_{50} were calculated. The distribution range of R_{max} in the study area is from 1.53 μm to 47.522 μm, and the average value is 16.2 μm. R_{50} ranges from 0.1 μm to 26 μm, and the average value is 5.87 μm.

The minimum flow pore-throat radius R_{min} [60] represents the minimum channel that can both store and percolate oil and gas, and it is an important indicator reflecting the lower limit of petrophysical properties. Based on MICP data, we take the Wells and Amaefule method [61] to calculate R_{min}. The Wells and Amaefule method calculates the contribution rate of permeability ΔK_i and cumulative contribution rate ΣK in each equaled pore volume interval. When the final ΣK reaches a certain percentage, the pore-throat radius corresponding to that last pore volume interval is R_{min}.

$$\Delta K_i = \frac{(2i-1)r_i^2}{\sum_{i=1}^{n}(2i-1)r_i^2} \times 100\% \qquad \sum K = \sum_{i=1}^{n} \Delta K_i \tag{2}$$

where i is the number of equaled pore volume interval, r_i is the pore-throat radius of each interval. The R_{min} of 4628 groups of core samples were finally calculated. The distribution range of R_{min} in the study area is from 0.03 μm to 4.18 μm. The average value is 0.63 μm.

After sorting, analyzing and calculating various parameters, 1523 groups of available data were finally selected from the database to be the dataset for predicting the pore-throat radius using a deep neural network. Each group of data includes seven parameters, that is, lithology, porosity, permeability, shale volume, R_{max}, R_{50}, and R_{min}, obtained from one core sample. Data preprocessing is one of the key procedures to improve DNN prediction accuracy. The dataset includes two types of parameters; one is lithology, which belongs to discrete variables, and the other is continuous variables such as porosity, permeability, pore-throat radius, etc. One-hot Encoding processing was performed for discrete variables to transform their categorical feature (for instance, 1, 2, 3) into a numerical feature (for instance, 001, 010, 100), which avoids unnecessary errors due to their classification attributes. For continuous variables, we performed Z-score standardization:

$$x = \frac{x - \mu}{\sigma} \tag{3}$$

where μ is the mathematical expectation of x, and σ is the standard deviation. The data standardized by Z-score conforms to the Gaussian distribution relationship, while eliminating the impact of different dimensions.

3.2. Deep Neural Network

The DNN structure includes one input layer, multiple hidden layers, and one output layer. The layers are fully connected [62], and the inputs of each current layer are the linear combination of the outputs of the previous layer. The inputs of each layer node are nonlinearly activated by the activation function, thereby enabling the network to output complex nonlinear mapping relationships [63,64]. For deep neural networks, there are more hidden layers than in a traditional BP neural network, and they can mine deeper high-order correlations between input and output variables [65,66]. Figure 4 shows a schematic diagram of the deep neural network used in this study.

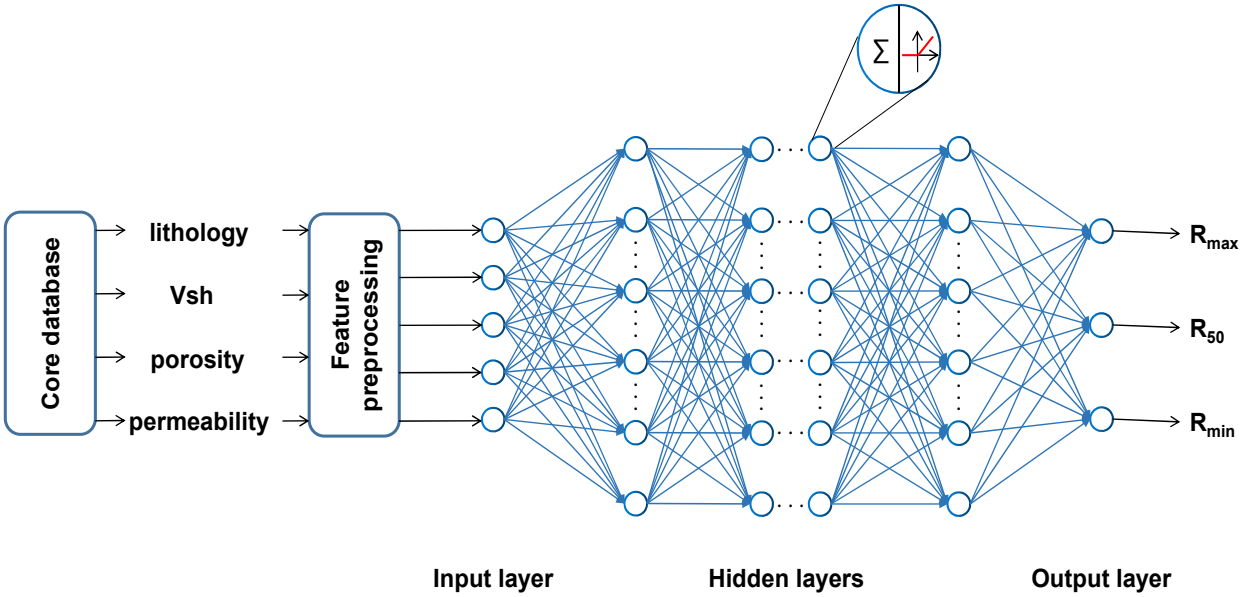


Figure 4. Schematic structure of the deep neural network in this study. The enlarged layer node displays the contained activation function.

From the scope of deep learning, the prediction of pore-throat radius belongs to a regression problem. This study comprehensively discusses the prediction results using evaluation metrics, including mean absolute error (*MAE*), root-mean-square error (*RMSE*), and mean absolute percentage error (*MAPE*):

Mean absolute error (*MAE*):

$$MAE = \frac{1}{N}\sum_{i=1}^{N}|(f_i - y_i)| \tag{4}$$

Root-mean-square error (*RMSE*):

$$RMSE = \sqrt{\frac{1}{N}\sum_{i=1}^{N}(f_i - y_i)^2} \tag{5}$$

Mean absolute percentage error (*MAPE*):

$$MAPE = \frac{1}{N}\sum_{i=1}^{N}\left|\frac{f_i - y_i}{y_i}\right| \times 100\% \tag{6}$$

where f_i is the predicted value, y_i is the true value, and N is the number of predicted samples.

3.3. Selection of DNN Key Elements

To improve the performance of the DNN model, some important elements involved should be optimally selected in combination with geological knowledge and actual data in the model.

3.3.1. Activation Function Selection

Activation function is a key element for a DNN model to achieve nonlinear mapping. The inputs of each layer node are transformed by the activation function and output to the next layer nodes. Currently, common activation functions include the Sigmoid activation function, the Tanh activation function, the ReLU activation function, and the Softmax activation function. Among them, the ReLU (Rectified Linear Unit) activation function is the most widely used function. It is non-saturated, hence the vanishing gradient problem

can be avoided. Moreover, due to the simple thresholding, the ReLU is computationally efficient [67,68]. Considering the principles of each activation function as well as compatibility with this study, the ReLU activation function was selected.

3.3.2. Loss Function Selection

The objective of the loss function is to minimize the prediction error. Common loss functions for regression problem include L1 loss (mean absolute error, MAE) and L2 loss (mean square error, MSE). As a loss function, MSE is easy to converge, and MAE is more robust to outliers. To combine the advantages of the two loss functions, the Huber loss function is proposed [69,70]:

$$L(y, f(x)) = \begin{cases} \frac{1}{2}(y - f(x))^2, & for\ |y - f(x)| < \delta \\ \delta|y - f(x)| - \frac{1}{2}\delta^2, & otherwise \end{cases} \quad (7)$$

where $f(x)$ is the predicted value, y is the true value, and δ is a hyperparameter. When δ is approximate to zero, the Huber loss tends to MAE; When δ is approximate to infinity, the Huber loss tends to MSE. In practice, in order to reduce the impact of outliers in the dataset, it is necessary to set the value of δ reasonably based on geological knowledge and the main distribution range of the pore-throat radius data. In general, setting δ at the upper limit of the main distribution range is a good choice.

To evaluate and choose the optimal loss function, we run the DNN model to calculate loss values of the R_{50} validation set by different loss functions, with other parameter settings unchanged (Table 3).

Table 3. Comparison of loss value by different loss functions.

Loss Function	Value
Huber	2.41
MSE (L2)	3.83
MAE (L1)	2.97

From Table 3, the Huber loss function has the lowest loss value, which conforms to the above analysis. Therefore, Huber loss is used as the loss function here.

3.3.3. Optimization Algorithm Selection

The optimization algorithm aims to find a set of weight values that minimize the loss function. From the perspective of convergence speed, the gradient descent algorithm and related extensions are commonly used for current deep learning. The idea of the gradient descent algorithm is to find the direction of the maximum gradient at each point of the function, and to iterate in that direction to the global minimum.

In order to determine the optimization algorithm suitable for this study from the main gradient descent algorithms including the fine-tuned stochastic gradient descent (SGD), AdaGrad, RMSprop, and Adam, we evaluated the loss values of the training set and validation set by the optimization algorithms (Figure 5), with other parameter settings unchanged.

From the comparison results, it can be seen that, in the training set (Figure 5a), Adam, fine-tuned SGD and RMSprop have relatively low loss values. In the validation set (Figure 5b), fine-tuned SGD has the smallest validation loss (val_loss) value. That means fine-tuned SGD performs best both in generalization and accuracy. Therefore, fine-tuned SGD was selected as the optimization algorithm for this study. The final selected elements of the deep neural network are shown in Table 4.

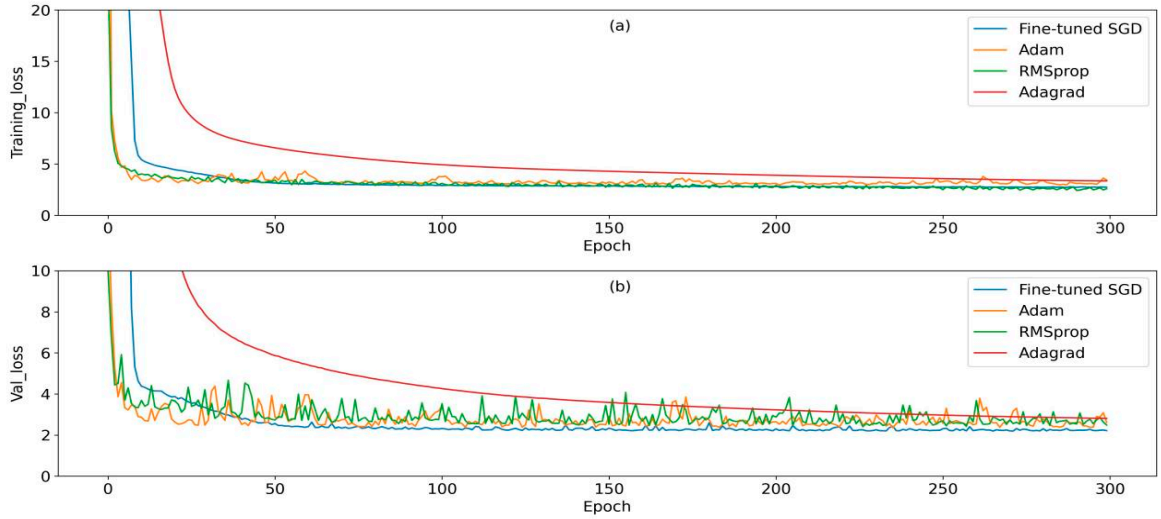


Figure 5. Comparison of accuracy by different optimization algorithms. (**a**) Training_loss, (**b**) Val_loss.

Table 4. Elements of the deep neural network model.

Data Preprocessing		Activation Function	Evaluation Metrics	Optimization Algorithm	Loss Function	Cross Validation	Regularization Method
Discrete Variable	Continuous Variable						
one-hot encoding	Z-score standardization	ReLU	RMSE, MAE, MAPE	Fine-tuned SGD	Huber loss	10-fold Stratified K-Fold	ReduceLROnPlateauEarlyStopping

3.4. Pore-Throat Radius Prediction by Deep Neural Network

A total of 1523 groups of data were available for this study. One tenth of the data (152 groups) was selected to be the test set by random sampling, which do not participate in training throughout the process and evaluate the prediction accuracy as the benchmark data.

The remaining 1371 groups of data were used as the training set. Considering the maldistribution of lithologic data, a 10-fold Stratified K-Fold cross validation was used to split a portion of the training set into a validation set. The validation set is only used to adjust the structures and parameters of the deep neural network at the end of each epoch, as well as evaluate the performance of the DNN.

It can be seen that the distribution range of the three porethroat radii is obviously different. Therefore, the deep neural network hyperparameters are set for each type of porethroat radius, respectively (Table 5). The main difference among hyperparameters is the epoch number and batch size. The optimal value is obtained through ReduceLROnPlateau and EarlyStopping in the regularization method of Keras 2.10.0 software library.

Table 5. Structural hyperparameter setting of the deep neural network.

Structural Hyperparameter	Value		
	R_{max}	R_{50}	R_{min}
Hidden layers	7		
Nodes of each layer	16, 64, 128, 128, 64, 64, 32		
Initial learning rate	0.001		
Epochs	100	200	140
Batch size	300	50	200

The deep neural network imports the training set into the network, and then trains the network layer by layer to the output through forward propagation to obtain the predicted value of the pore-throat radius. Then, the predicted error of each layer node is calculated by the Huber loss function during back propagation. Meanwhile, SGD with momentum is used to adjust the model weight by calculating the gradient of each parameter of the model, make the prediction of validation set close to the target, i.e., the true pore-throat radius. With multiple epochs iterating, a trained deep neural network model is complete.

The predicted values of R_{max}, R_{50}, and R_{min} are obtained by using the trained DNN model on the test set.

3.5. Pore-Throat Radius Prediction by Comparable Machine Learning Methods

In order to verify the effect of the DNN model more comprehensively, we selected three mature machine learning algorithms, i.e., Support Vector Regression (SVR), Random Forest Regression (RFR) and XGBoost Regression (XGBR), which have been proved to be effective in petrophysical characterization and microscopic heterogeneity [51–53], to synchronously predict the pore-throat radius. Support Vector Regression, which is derived from Support Vector Machine, is used to find a hyper-plane that has the smallest margin of ε deviation from the actually obtained targets [71]; meanwhile, the ε tube needs to involve the maximum number of training data. The kernel functions extend the SVR to deal with nonlinear correlations by mapping low-dimensional linearly inseparable data to high-dimensional linearly separable space. Random Forest and XGBoost, which belong to Ensemble Learning, consist of numerous Decision Tree (DT) algorithms as weak learners; the results of these weak learners are assembled to gain a better performance. The difference between Random Forest and XGBoost is ensemble procedure. Random Forest uses a Bagging procedure; it randomly resamples a portion of the original dataset with replacements, concurrently run DT weak learners and averages the results as the ultimate prediction. XGBoost uses a Boosting procedure, which takes the whole dataset into account, sequentially and iteratively adds the results of each DT weak learner, meanwhile adjusting weights of samples and weak learners as per the last regression. In parameter setting, by grid search and cross validation, SVR adopts a radial basis function (rbf) as the kernel function; the kernel coefficient γ is set to auto mode, regularization parameter C is set to 100. RFR consists of 300 DTs; the criterion uses MSE, max_depth is set to none. XGBR consists of 1000 DTs, max_depth is set to 7, eta is set to 0.1, subsample is set to 0.7, and colsample_bytree is set to 1. These three comparable methods have the same epoch numbers and batch size with the DNN method.

The R_{max}, R_{50}, and R_{min} of the test set are predicted by these fine-tuned comparable methods.

3.6. Pore-Throat Radius Prediction by J-Function Method

The J-function method can be used to obtain the capillary pressure curve of unmeasured rocks by fitting the known capillary pressure curve; thereby the pore-throat radius can be derived. There is a large amount of MICP experimental data in the study area, so the J-function method is preferred for obtaining the pore-throat radius of unmeasured cores.

$$J(S_{wD}) = 0.086 p_{cHg}(S_{wD}) \sqrt{\frac{k}{\varphi}} \tag{8}$$

where S_{wD} is the normalized water saturation, k is the permeability, φ is the porosity, $p_{cHg}(S_{wD})$ is the capillary pressure, and $J(S_{wD})$ is the J-function value of the rock sample. For any unmeasured core or location with known porosity, permeability, and connate water saturation (initial oil saturation), the corresponding capillary pressure curve (equal to the MICP curve) can be obtained after fitting the relationship between $J(S_{wD})$ and S_{wD}, and then by using Equations (1) and (2), the predicted value of R_{max}, R_{50}, and R_{min} is achievable.

Due to the differences in petrophysical properties and pore structure characteristics, the J-function needs to be fitted respectively by lithology. The fitting results show that the accuracy of each curve can meet the subsequent calculation requirements (Figure 6).

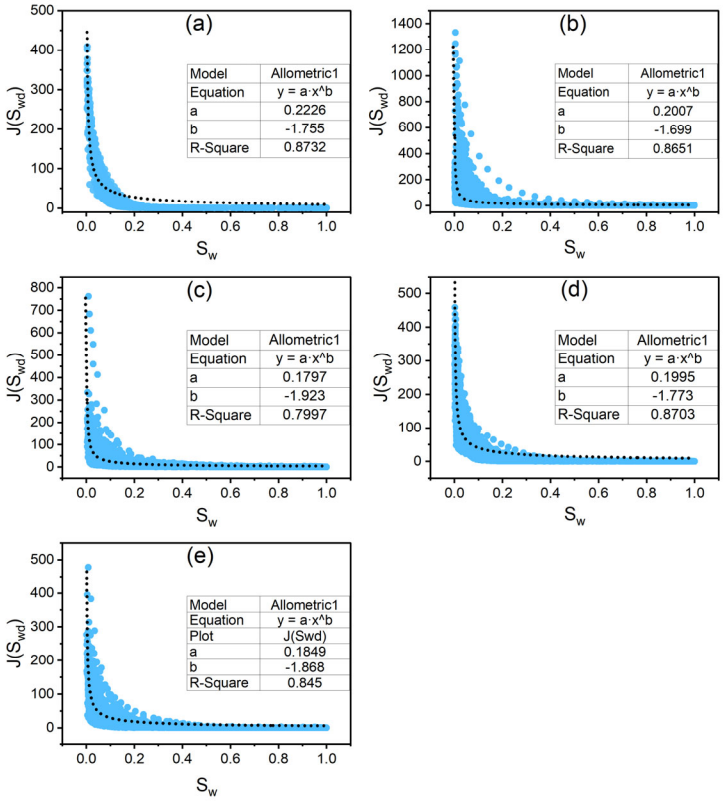


Figure 6. The J-function relationship and fitting equation of each lithology. (**a**) Results of the medium sandstone, (**b**) results of the fine sandstone, (**c**) results of the siltstone, (**d**) results of the unequal-grained sandstone, (**e**) results of the diamictite.

The R_{max}, R_{50}, and R_{min} values of the test set are calculated by using the fitted J-functions.

4. Results and Discussion

4.1. Predictive Performance Analysis

Theoretically, the deep neural network is a type of deep learning method, and deep learning is a branch of machine learning. In comparison with machine learning methods, the DNN has a more complex network structure and more network nodes, and with these it can process and predict more complicated data. The root-mean-square error (RMSE) and mean absolute error (MAE) of the prediction results which derived from the deep neural network model, Support Vector Regression (SVR), Random Forest Regression (RFR), XGBoost Regression (XGBR), and the J-function method are shown in Figure 7. From all perspectives, the deep neural network model achieves the best prediction performance. In Figure 7a,b, the involved machine learning methods are better-performing than the J-function method, with regards to the deep neural network model; the RMSE of R_{max}, R_{50} and R_{min} are 3.27 μm, 1.25 μm and 0.35 μm, decreasing by 46%, 57.8% and 14%, respectively, when compared with the J-function method; the MAE of R_{max}, R_{50} and R_{min} are 2.27 μm, 0.77 μm and 0.18 μm, decreasing by 47.4%, 64.3% and 32.4%, respectively, when compared with the J-function method. Among machine learning methods, SVR and RFR have similar effects, while both of them perform more strongly than XGBR, but the proposed DNN is obviously outstanding. This indicates that the fine-tuned DNN model can better fit the nonlinear relationship between geological parameters and pore-throat radius.

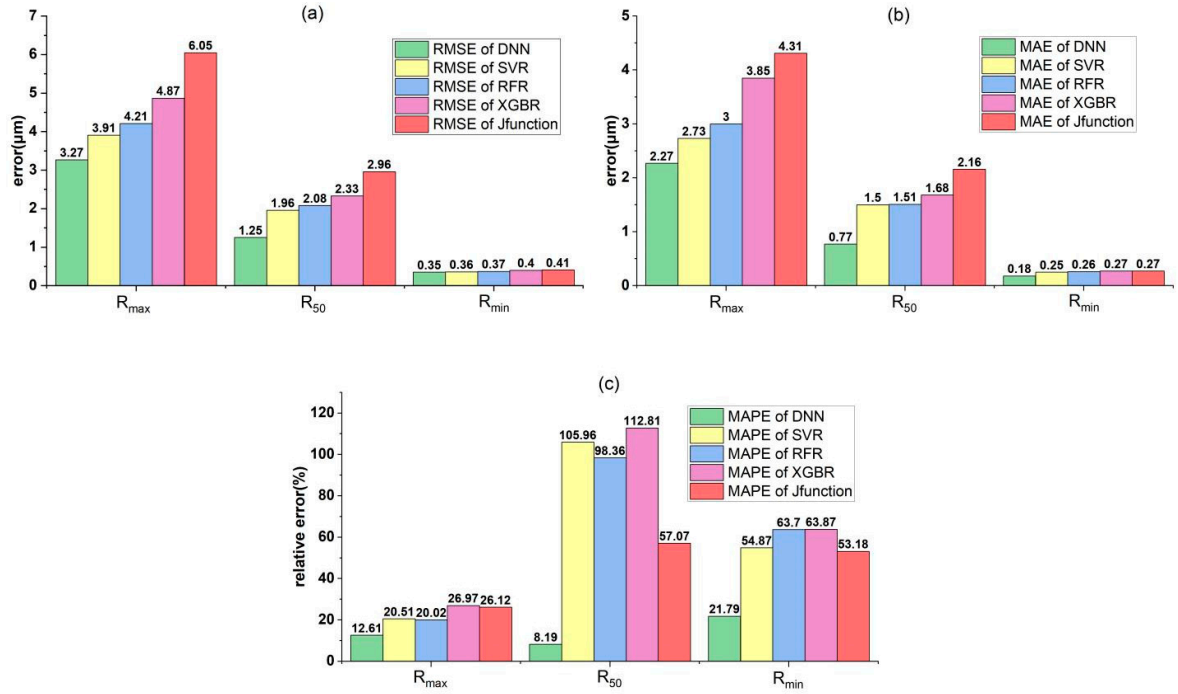


Figure 7. Comparison of RMSE/MAE/MAPE of DNN, SVR, RFR, XGBR and J-function prediction results. (**a**) RMSE, (**b**) MAE, (**c**) MAPE.

The dimension of RMSE and MAE is consistent with that of the target variable, i.e., the pore-throat radius. As can be seen from Equations (4) and (5), the distinction between two evaluation metrics is that RMSE is more sensitive to outliers than MAE, and therefore, RMSE is generally larger than MAE. In this study, the difference value between the RMSE and MAE of the deep neural network is significantly smaller than that of the other four methods, indicating that the distribution of the DNN predicted value is closer to the true value distribution, showing a better prediction ability.

Figure 7c shows the mean absolute percentage error (MAPE) of the deep neural network model and other comparable methods. Dimensionless MAPE is an evaluation metric that represents relative error. It can analyze the prediction performance from another perspective. The MAPE of the DNN model for predicting R_{max}, R_{50} and R_{min} are 12.61%, 8.19%, and 21.79%, respectively. Compared with the J-function method, the MAPE is significantly reduced, and the prediction accuracy of R_{max}, R_{50}, and R_{min} is improved by 13.5%, 48.9%, and 31.4%, respectively. The MAPE of SVR, RFR and XGBR for predicting R_{50} and R_{min} are unduly high; this indicates that small values of pore-throat radius are not well-predicted by these methods.

Through the analysis of the above evaluation metrics, the deep neural network model shows better results in predicting R_{max}, R_{50}, and R_{min} than comparable machine learning methods and the existing conventional J-function method. Among them, the prediction of R_{max} and R_{50} has achieved high accuracy. That said, from the perspective of MAPE, there is room for improvement in the prediction accuracy of R_{min}. This is mainly due to the small value of R_{min}; a tiny error could cause obvious fluctuation in MAPE. However, it is still more accurate than the other four methods, and it has been able to meet the requirements of subsequent work including water shutoff and chemical flooding-plugging, as well as oil-displacing agent slug optimization.

Aside from the evaluation metrics analysis, we collected the running time of each method (Table 6). It can be seen from Table 6 that, due to its structural complexity, the training and predicting time of the DNN model are the longest among machine learning methods, but the differential can be ignored since it is less than a minute. The conventional J-function method is very time-consuming.

Table 6. The running time of each method.

Method	Running Time for Training (s)	Running Time for Predicting (s)
DNN	51.34	3.44
SVR	34.81	2.56
RFR	29.73	3.15
XGBR	33.58	2.92
J-function	/	>3600

4.2. Analysis of Actual Prediction

The trained deep neural network model has predicted the R_{max}, R_{50}, and R_{min} of 152 core samples in the test set. Due to the random sampling of the dataset, the number of core samples from the same well which are assigned to the test set is stochastic. To be more persuasive, we chose Well X6-P35H with 19 (the most in the test set) groups of cores to analyze the DNN predicted results. Figure 8 shows the true values and prediction results of the DNN model, SVR, RFR, XGBR and J-function method in Well X6-P35H, respectively. Table 7 gives the mean absolute errors of the 19 groups of core samples in Well X6-P35H as predicted by the DNN model, SVR, RFR, XGBR and J-function method.

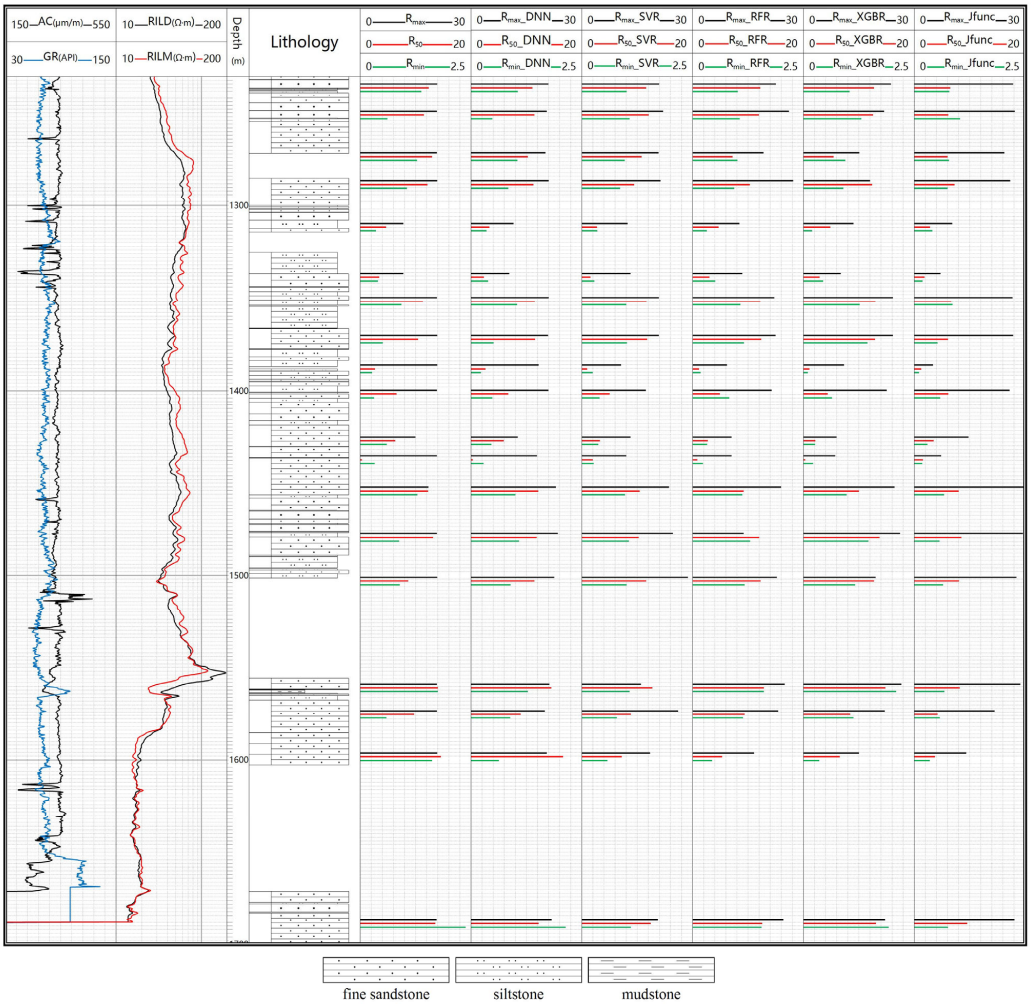


Figure 8. Prediction results of DNN model, SVR, RFR, XGBR and J-function method for Well X6-P35H. To illustrate the R_{max}, R_{50}, and R_{min} of each core sample more clearly, the R_{50} (red line), and R_{min} (green line) are drawn by slightly deviating from the true depth at which the R_{max} (black line) located.

Table 7. The mean absolute errors of each method in prediction of Well X6-P35H.

Mean Absolute Errors	Methods				
	DNN	**SVR**	**RFR**	**XGB**	**J-Function**
R_{max}	1.195	3.034	4.012	4.176	6.410
R_{50}	0.951	2.007	2.028	2.072	4.093
R_{min}	0.207	0.329	0.351	0.406	0.434

The black line, red line and green line in Figure 8 represent R_{max}, R_{50} and R_{min}, respectively. The depth of the core samples from Well X6-P35H ranges from 1235 m to 1687 m, and such a large depth-range includes different lithologies, which makes these core samples representative. On the whole, the DNN model has the best prediction performance, and can better match the variation trend of the true pore-throat radius value compared with other methods (Figure 8, Table 7). In well X6-P35H, the R_{max} of fine sandstone, most of which are about 20 μm, are relatively stable, but the prediction results of the SVR, RFR, XGBR and J-function are obviously larger than the true values of $R_{max;}$ in contrast, the prediction results of the DNN model show little fluctuation, which is most consistent with the true values of R_{max}. With regard to the prediction of R_{50} and R_{min}, the performance of SVR, RFR and XGBR is more unstable than the DNN model and has greater errors; meanwhile, the prediction of the J-function is apparently small. Therefore, the optimized and fine-tuned DNN model can accurately predict the pore-throat radius of the reservoir, which provides an important basis for the subsequent fine microscopic heterogeneity characterization.

5. Conclusions

The pore-throat radius is one of the key parameters for characterizing microscopic heterogeneity, The current mainstream methods are mainly aimed at characterizing it. In this study, based on the core analysis database, a fine-tuned deep neural network model is proposed to accurately predict the maximum pore-throat radius, the median pore-throat radius, and the minimum flow pore-throat radius for the first time. In the process of constructing the deep neural network model, we have brought in geological thinking and optimized the components and hyperparameters of the deep neural network. By training and validating the DNN model, the optimal hyperparameter combination for each type of pore-throat radius is given. This study provides a reference for the combination of deep learning and expertise on the oil and gas field.

Core samples of the Q Oilfield in Songliao Basin are employed to evaluate SVR, RFR, XGBR, J-function and the proposed fine-tuned DNN model; the evaluation metrics show that the DNN model outperforms the other methods in predicting R_{max}, $R_{50,}$ and $R_{min;}$ the root-mean-square error (RMSE), mean absolute error (MAE) and mean absolute percentage error (MAPE) are decreased by 14–57.8%, 32.4–64.3% and 13.5–48.9%, respectively. The prediction results reveal that the DNN model is more stable and can better match the variation trend of the true pore-throat radius value, which demonstrates the effectiveness and advancement of our DNN model. This will provide effective support for the remaining oil characterization.

This study is the first step for establishing a full-scale characterization of the microscopic pore structure of reservoirs, and subsequent work will focus on predicting the microscopic pore-throat radius of a single well scale by deep learning.

Author Contributions: Conceptualization, Y.H.; Methodology, Y.H., S.L. and H.W.; Investigation, Y.H.; Software, Y.H.; Writing-original draft, Y.H.; Visualization, Y.H.; Supervision, S.L., H.W. and P.L.; Resources, S.L.; Project administration, H.W.; Writing—review & editing, P.L.; Data curation, Y.C. All authors have read and agreed to the published version of the manuscript.

Funding: This work was supported by the Key Laboratory of Marine Reservoir Evolution and Hydrocarbon Enrichment Mechanism (Ministry of Education), China University of Geosciences (Beijing) (Grant No. 2019JYB02001).

Data Availability Statement: The data of this study will be made available on request.

Acknowledgments: The authors express their sincere thanks to the Key Laboratory of Marine Reservoir Evolution and Hydrocarbon Enrichment Mechanism. Thanks to the Research Institute of Petroleum Exploration and Development, PetroChina, for providing core data.

Conflicts of Interest: The authors declare no conflict of interest.

References

1. Morrow, N.R. Small-scale packing heterogeneities in porous sedimentary rocks. *AAPG Bull.* **1971**, *55*, 514–522.
2. Pettijohn, F.J.; Potter, P.E.; Siever, R. *Sand and Sandstone*; Springer Science & Business Media: Berlin/Heidelberg, Germany, 2012.
3. Yinan, Q. Developments in reservoir sedimentology of continental clastic rocks in China. *Acta Sedimentol. Sin.* **1992**, *10*, 16–24.
4. Li, J.; Liu, Y.; Gao, Y.; Cheng, B.; Meng, F.; Xu, H. Effects of microscopic pore structure heterogeneity on the distribution and morphology of remaining oil. *Pet. Explor. Dev.* **2018**, *45*, 1112–1122. [CrossRef]
5. Liu, G.; Xie, S.; Tian, W.; Wang, J.; Li, S.; Wang, Y.; Yang, D. Effect of pore-throat structure on gas-water seepage behaviour in a tight sandstone gas reservoir. *Fuel* **2022**, *310*, 121901. [CrossRef]
6. Yuan, C.; Pu, W.; Varfolomeev, M.A.; Wei, J.; Zhao, S.; Cao, L.N. Deformable microgel for enhanced oil recovery in high-temperature and ultrahigh-salinity reservoirs: How to design the particle size of microgel to achieve its optimal match with pore throat of porous media. *SPE J.* **2021**, *26*, 2053–2067. [CrossRef]
7. Gao, Z.; Hu, Q. Estimating permeability using median pore-throat radius obtained from mercury intrusion porosimetry. *J. Geophys. Eng.* **2013**, *10*, 025014. [CrossRef]
8. Lala, A.M.S.; El-Sayed, N.A. Controls of pore throat radius distribution on permeability. *J. Pet. Sci. Eng.* **2017**, *157*, 941–950. [CrossRef]
9. Gong, Y.; Liu, K.; Zhuo, Q. Pore throat radius cutoffs from depression to uplift zones: A case study of the tight oil reservoir from the Songliao Basin, NE China. *J. Asian Earth. Sci.* **2023**, *246*, 105576. [CrossRef]
10. Xiao, Q.; Wang, Z.; Yang, Z.; Xiang, Z.; Liu, Z.; Yang, W. Novel method for determining the lower producing limits of pore-throat radius and permeability in tight oil reservoirs. *Energy. Rep.* **2021**, *7*, 1651–1656. [CrossRef]
11. Ali, L.; Barrufet, M.A. Study of pore structure modification using environmental scanning electron microscopy. *J. Pet. Sci. Eng.* **1995**, *12*, 323–338. [CrossRef]
12. Chandra, D.; Vishal, V. A critical review on pore to continuum scale imaging techniques for enhanced shale gas recovery. *Earth Sci. Rev.* **2021**, *217*, 103638. [CrossRef]
13. Hu, C.; Yang, F.; Ning, Z.; Wang, B.; Peng, K.; Liu, H. Characterization of microscopic pore structures in shale reservoirs. *Acta Pet. Sin.* **2013**, *34*, 301.
14. Ivanova, A.; Mitiurev, N.; Cheremisin, A.; Orekhov, A.; Kamyshinsky, R.; Vasiliev, A. Characterization of organic layer in oil carbonate reservoir rocks and its effect on microscale wetting properties. *Sci. Rep.* **2019**, *9*, 10667. [CrossRef]
15. Yang, X.; Wang, J.; Zhu, C.; He, M.; Gao, Y. Effect of wetting and drying cycles on microstructure of rock based on SEM. *Environ. Earth Sci.* **2019**, *78*, 183. [CrossRef]
16. Clarkson, C.; Solano, N.; Bustin, R.; Bustin, A.; Chalmers, G.; He, L.; Melnichenko, Y.; Radliński, A.; Blach, T. Pore structure characterization of North American shale gas reservoirs using USANS/SANS, gas adsorption, and mercury intrusion. *Fuel* **2013**, *103*, 606–616. [CrossRef]
17. Shaobo, T.H.Z.S.L.; Hong, Z. Determination of organic-rich shale pore features by mercury injection and gas adsorption methods. *Acta Pet. Sin.* **2012**, *33*, 419.
18. Timur, A. Pulsed nuclear magnetic resonance studies of porosity, movable fluid, and permeability of sandstones. *J. Pet. Technol.* **1969**, *21*, 775–786. [CrossRef]
19. Golsanami, N.; Sun, J.; Zhang, Z. A review on the applications of the nuclear magnetic resonance (NMR) technology for investigating fractures. *J. Appl. Geophys.* **2016**, *133*, 30–38. [CrossRef]
20. Arns, C.H.; Bauget, F.; Sakellariou, A.; Senden, T.J.; Sheppard, A.P.; Sok, R.M.; Ghous, A.; Pinczewski, W.V.; Knackstedt, M.A.; Kelly, J.C. Digital core laboratory: Petrophysical analysis from 3D imaging of reservoir core fragments. *Petrophysics* **2005**, *46*, 260–277.
21. Knackstedt, M.A.; Arns, C.H.; Limaye, A.; Sakellariou, A.; Senden, T.J.; Sheppard, A.P.; Sok, R.M.; Pinczewski, W.V.; Bunn, G.F. Digital Core Laboratory: Properties of reservoir core derived from 3D images. In Proceedings of the SPE Asia Pacific Conference on Integrated Modelling for Asset Management, Kuala Lumpur, Malaysia, 29–30 March 2004.
22. Arns, C.H.; Knackstedt, M.A.; Pinczewski, W.; Martys, N.S. Virtual permeametry on microtomographic images. *J. Pet. Sci. Eng.* **2004**, *45*, 41–46. [CrossRef]
23. Fredrich, J.; Menéndez, B.; Wong, T.-F. Imaging the pore structure of geomaterials. *Science* **1995**, *268*, 276–279. [CrossRef] [PubMed]

24. Zhao, J.; Cui, L.; Chen, H.; LI, N.; Wang, Z.; Ma, Y.; Du, G. Quantitative characterization of rock microstructure of digital core based on CT scanning. *Geoscience* **2020**, *34*, 1205.
25. Okabe, H.; Blunt, M.J. Pore space reconstruction using multiple-point statistics. *J. Pet. Sci. Eng.* **2005**, *46*, 121–137. [CrossRef]
26. Arand, F.; Hesser, J. Accurate and efficient maximal ball algorithm for pore network extraction. *Comput. Geosci.* **2017**, *101*, 28–37. [CrossRef]
27. Al-Kharusi, A.S.; Blunt, M.J. Network extraction from sandstone and carbonate pore space images. *J. Pet. Sci. Eng.* **2007**, *56*, 219–231. [CrossRef]
28. Liu, J.; Regenauer-Lieb, K. Application of percolation theory to microtomography of rocks. *Earth Sci. Rev.* **2021**, *214*, 103519. [CrossRef]
29. Borello, E.S.; Peter, C.; Panini, F.; Viberti, D. Application of A* algorithm for microstructure and transport properties characterization from 3D rock images. *Energy* **2022**, *239*, 122151. [CrossRef]
30. Liang, Y.; Hu, P.; Wang, S.; Song, S.; Jiang, S. Medial axis extraction algorithm specializing in porous media. *Powder Technol.* **2019**, *343*, 512–520. [CrossRef]
31. Rabbani, A.; Mostaghimi, P.; Armstrong, R.T. Pore network extraction using geometrical domain decomposition. *Adv. Water Resour.* **2019**, *123*, 70–83. [CrossRef]
32. Xiao, Q.; Yang, Z.; Wang, Z.; Qi, Z.; Wang, X.; Xiong, S. A full-scale characterization method and application for pore-throat radius distribution in tight oil reservoirs. *J. Pet. Sci. Eng.* **2020**, *187*, 106857. [CrossRef]
33. Qu, Y.; Sun, W.; Wu, H.; Huang, S.; Li, T.; Ren, D.; Chen, B. Impacts of pore-throat spaces on movable fluid: Implications for understanding the tight oil exploitation process. *Mar. Pet. Geol.* **2022**, *137*, 105509. [CrossRef]
34. Wei, Q.; Li, X.; Zhang, J.; Hu, B.; Zhu, W.; Liang, W.; Sun, K. Full-size pore structure characterization of deep-buried coals and its impact on methane adsorption capacity: A case study of the Shihezi Formation coals from the Panji Deep Area in Huainan Coalfield, Southern North China. *J. Pet. Sci. Eng.* **2019**, *173*, 975–989. [CrossRef]
35. Brooks, R.H. *Hydraulic Properties of Porous Media*; Colorado State University: Fort Collins, CO, USA, 1965.
36. Leverett, M. Capillary behavior in porous solids. *Trans. AIME* **1941**, *142*, 152–169. [CrossRef]
37. Aguilera, R. Incorporating capillary pressure, pore throat aperture radii, height above free-water table, and winland r 35 values on Pickett plots. *AAPG Bull.* **2002**, *86*, 605–624.
38. Kolodzie, S. Analysis of pore throat size and use of the Waxman-Smits equation to determine OOIP in Spindle Field, Colorado. In Proceedings of the SPE Annual Technical Conference and Exhibition, Dallas, TX, USA, 21–24 September 1980.
39. Ziarani, A.S.; Aguilera, R. Pore-throat radius and tortuosity estimation from formation resistivity data for tight-gas sandstone reservoirs. *J. Appl. Geophys.* **2012**, *83*, 65–73. [CrossRef]
40. Yu, S.; Ma, J. Deep learning for geophysics: Current and future trends. *Rev. Geophys.* **2021**, *59*, e2021RG000742. [CrossRef]
41. Saikia, P.; Baruah, R.D.; Singh, S.K.; Chaudhuri, P.K. Artificial Neural Networks in the domain of reservoir characterization: A review from shallow to deep models. *Comput. Geosci.* **2020**, *135*, 104357. [CrossRef]
42. Li, Y.; Lian, P.Q.; Xue, Z.J.; Dai, C. Application status and prospect of big data and artificial intelligence in oil and gas field development. *J. China Univ. Pet. Ed. Nat. Sci.* **2020**, *44*, 1–11.
43. Wolpert, D.H. The lack of a priori distinctions between learning algorithms. *Neural Comput.* **1996**, *8*, 1341–1390. [CrossRef]
44. Naeini, E.Z.; Green, S.; Russell-Hughes, I.; Rauch-Davies, M. An integrated deep learning solution for petrophysics, pore pressure, and geomechanics property prediction. *Lead. Edge* **2019**, *38*, 53–59. [CrossRef]
45. Li, T.; Wang, Z.; Wang, R.; Yu, N. Pore type identification in carbonate rocks using convolutional neural network based on acoustic logging data. *Neural Comput. Appl.* **2021**, *33*, 4151–4163. [CrossRef]
46. Miller, R.S.; Rhodes, S.; Khosla, D.; Nino, F. Application of artificial intelligence for depositional facies recognition-Permian basin. In Proceedings of the SPE/AAPG/SEG Unconventional Resources Technology Conference, Denver, CO, USA, 22–24 July 2019.
47. Pham, N.; Wu, X.; Zabihi Naeini, E. Missing well log prediction using convolutional long short-term memory network. *Geophysics* **2020**, *85*, WA159–WA171. [CrossRef]
48. Zhang, D.; Yuntian, C.; Jin, M. Synthetic well logs generation via Recurrent Neural Networks. *Pet. Explor. Dev.* **2018**, *45*, 629–639. [CrossRef]
49. Gao, X.; He, W.; Hu, Y. Modeling of meandering river deltas based on the conditional generative adversarial network. *J. Pet. Sci. Eng.* **2020**, *193*, 107352. [CrossRef]
50. Zhang, T.-F.; Tilke, P.; Dupont, E.; Zhu, L.-C.; Liang, L.; Bailey, W. Generating geologically realistic 3D reservoir facies models using deep learning of sedimentary architecture with generative adversarial networks. *Pet. Sci.* **2019**, *16*, 541–549. [CrossRef]
51. Lu, H.; Hu, S.; Zhang, L.; Tang, H.; Yang, T.; Zhao, Y.; Li, L.; Zhao, F. Prediction of the pore structure by machine learning techniques in the carbonate reservoirs in Iraq H oilfield. *Geol. J.* **2023**, *58*, 2427–2437. [CrossRef]
52. Wang, Y.; Sun, S. Multiscale pore structure characterization based on SEM images. *Fuel* **2021**, *289*, 119915. [CrossRef]
53. Pan, S.; Zheng, Z.; Guo, Z.; Luo, H. An optimized XGBoost method for predicting reservoir porosity using petrophysical logs. *J. Pet. Sci. Eng.* **2022**, *208*, 109520. [CrossRef]
54. Alqahtani, N.; Alzubaidi, F.; Armstrong, R.T.; Swietojanski, P.; Mostaghimi, P. Machine learning for predicting properties of porous media from 2d X-ray images. *J. Pet. Sci. Eng.* **2020**, *184*, 106514. [CrossRef]
55. Alqahtani, N.; Armstrong, R.T.; Mostaghimi, P. Deep learning convolutional neural networks to predict porous media properties. In Proceedings of the SPE Asia Pacific Oil and Gas Conference and Exhibition, Brisbane, Australia, 23–25 October 2018.

56. Misbahuddin, M. Estimating petrophysical properties of shale rock using conventional neural networks CNN. In Proceedings of the SPE Annual Technical Conference and Exhibition, Virtual, 26–29 October 2020.
57. Iraji, S.; Soltanmohammadi, R.; Matheus, G.F.; Basso, M.; Vidal, A.C. Application of unsupervised learning and deep learning for rock type prediction and petrophysical characterization using multi-scale data. *Geoenergy Sci. Eng.* **2023**, *230*, 212241. [CrossRef]
58. Zhou, Y.; Yin, D.; Cao, R.; Zhang, C. The mechanism for pore-throat scale emulsion displacing residual oil after water flooding. *J. Pet. Sci. Eng.* **2018**, *163*, 519–525. [CrossRef]
59. Washburn, E.W. Note on a method of determining the distribution of pore sizes in a porous material. *Proc. Natl. Acad. Sci. USA* **1921**, *7*, 115–116. [CrossRef] [PubMed]
60. Purcell, W. Capillary pressures-their measurement using mercury and the calculation of permeability therefrom. *J. Pet. Technol.* **1949**, *1*, 39–48. [CrossRef]
61. Wells, J.; Amaefule, J. Capillary pressure and permeability relationships in tight gas sands. In Proceedings of the SPE/DOE Low Permeability Gas Reservoirs Symposium, Denver, CO, USA, 19–22 May 1985.
62. Samek, W.; Montavon, G.; Lapuschkin, S.; Anders, C.J.; Müller, K.R. Explaining deep neural networks and beyond: A review of methods and applications. *Proc. IEEE* **2021**, *109*, 247–278. [CrossRef]
63. Nassif, A.B.; Shahin, I.; Attili, I.; Azzeh, M.; Shaalan, K. Speech recognition using deep neural networks: A systematic review. *IEEE Access* **2019**, *7*, 19143–19165. [CrossRef]
64. Srinidhi, C.L.; Ciga, O.; Martel, A.L. Deep neural network models for computational histopathology: A survey. *Med. Image Anal.* **2021**, *67*, 101813. [CrossRef]
65. Montavon, G.; Samek, W.; Müller, K.-R. Methods for interpreting and understanding deep neural networks. *Digit. Signal Process.* **2018**, *73*, 1–15. [CrossRef]
66. Sze, V.; Chen, Y.-H.; Yang, T.-J.; Emer, J.S. Efficient processing of deep neural networks: A tutorial and survey. *Proc. IEEE* **2017**, *105*, 2295–2329. [CrossRef]
67. Jiang, X.; Pang, Y.; Li, X.; Pan, J.; Xie, Y. Deep neural networks with elastic rectified linear units for object recognition. *Neurocomputing* **2018**, *275*, 1132–1139. [CrossRef]
68. Weng, L.; Zhang, H.; Chen, H.; Song, Z.; Hsieh, C.J.; Daniel, L.; Boning, D.; Dhillon, I. Towards fast computation of certified robustness for relu networks. In Proceedings of the 35th International Conference on Machine Learning, PMLR 80, Stockholm, Sweden, 10–15 July 2018.
69. Esmaeili, A.; Marvasti, F. A novel approach to quantized matrix completion using huber loss measure. *IEEE Signal Process. Lett.* **2019**, *26*, 337–341. [CrossRef]
70. Gupta, D.; Hazarika, B.B.; Berlin, M. Robust regularized extreme learning machine with asymmetric Huber loss function. *Neural Comput. Appl.* **2020**, *32*, 12971–12998. [CrossRef]
71. Smola, A.J.; Schölkopf, B. A tutorial on support vector regression. *Stat. Comput.* **2004**, *14*, 199–222. [CrossRef]

Disclaimer/Publisher's Note: The statements, opinions and data contained in all publications are solely those of the individual author(s) and contributor(s) and not of MDPI and/or the editor(s). MDPI and/or the editor(s) disclaim responsibility for any injury to people or property resulting from any ideas, methods, instructions or products referred to in the content.